Quarterly Status Report 5

Novel Investigation of Iron Cross Sections via Spherical Shell Transmission Measurements and Particle Transport Calculations for Material Embrittlement Studies

National Institute of Standards and Technology
The Pennsylvania State University
Ohio University

October 2000

Grant Number: USDE-DE-FG03-99SF21897

A. Fabrication of the Iron Spheres

Previously, measurements were made of the transmission of 14 MeV neutrons through various spherical shell thicknesses of iron in a comprehensive investigation at Lawrence Livermore National Laboratory (LLNL) about 30 years ago. Two of these spheres, composed of hemispherical sections, have appropriate dimensions for the lower energy neutron measurements that we propose to make. Due to their interest in our experimental results, LLNL has agreed to make these hemispheres available for our work. Those hemispheres have been shipped. In addition, a spherical iron shell, composed of two hemispherical sections with an annular thickness of approximately 1 inch, was fabricated at NIST. However, since we will need additional hemispheres for our experiments, we purchased a radius cutter that will allow us to fabricate hemispheres as large as 5" in radius at the Ohio University Machine Shop. This will give us maximum flexibility to adapt to the needs of the spherical shell transmission experiments. High purity (99.94% iron) Armco iron has been obtained which can be used to make the smaller hemispheres. Larger hemispheres will be made using ASTM designation steel with high iron content. In all cases compositional analyses will be made of the hemispheres.

B. Detector efficiency determination

Measurements were made of the source spectrum for several reactions which may be appropriate for this work. The most useful are the Be(d,n), B(d,n) and Al(d,n) reactions which are shown in Fig. 1. Though the intensities are somewhat more favorable for the Be(d,n) and B(d,n) reactions, the Al(d,n) reaction was chosen for this work, above 250

DISCLAIMER

DISCLAIMER

Portions of this document may be illegible in electronic image products. Images are produced from the best available original document.

keV, since there is less energy dependent structure in its spectra. The detector efficiencies have been determined well above about 250 keV. The spectra measurements were made relative to the $^{235}U(n,f)$ neutron cross section standard. Additional experimental work using the Be(p,n) reaction has allowed us to extend our procedure for obtaining absolute efficiencies of neutron detectors down to about 80 keV. Making efficiency measurements with white spectrum source reactions such as this removes one of the limitations on previous work, such as the LLNL experiment where the efficiency was determined at a limited number of isolated points with interpolation between those points. The efficiencies of the lithium glass and NE-213 detectors will be determined at the time of the experiment by using suitable white spectrum source reactions.

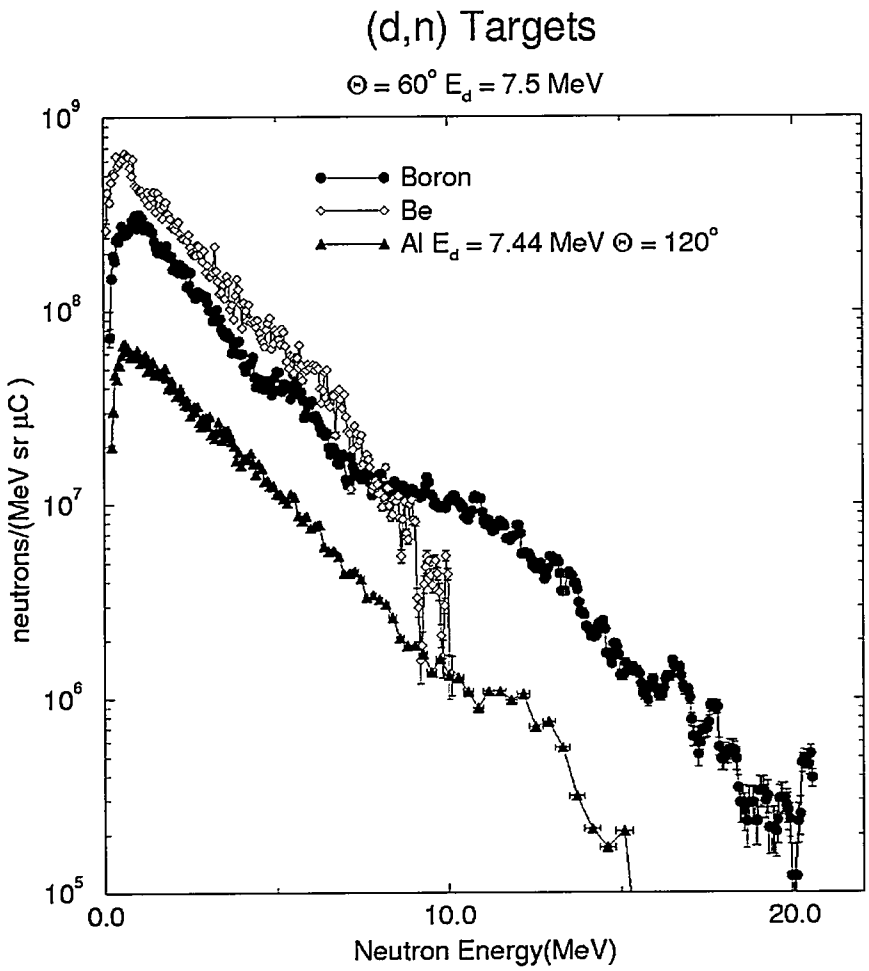

Figure 1: Neutron yields from deuterons on boron, beryllium and Aluminum

C. Development of analytical models

In this Section, we discuss our progress in modeling and analysis of the iron sphere experiment. We have performed a series of analyses and developed new methodologies for being able to perform accurate and efficient simulations for the design and analysis of the time-of-flight experiment.

In the remainder of the section we discuss the following: i) Development of a more efficient MCNP model; ii) MCNP analyses for different target shapes; iii) Development of a new version of MCNP for identifying particles that are scattered inelastically at the target and reached the detector; iv) Use of the new version of MCNP in optimizing the experimental setup; v) Development and benchmarking of 3-D PENTRAN models using a new methodology for generation of angular quadrature sets for reducing the ray-effects; vi) Development of new methodologies based on the PENTRAN S_N, ray-tracing in the air, and coupling of forward and adjoint S_N solutions. These new methodologies provide the possibility of performing detailed simulations and analyses accurately and efficiently.

i) Development of a more efficient MCNP model

Monte Carlo simulation of a very large model can be very expensive, hence we have examined two models: a full size model shown in Fig. 2, and a small model shown in Fig. 3.

The full size model has the following dimensions:

- Overall size = 108.6 x 153.6 x 626 cm^3
- Wall thickness = 122.0 cm
- Hole diameter = 30 cm
- Thickness of the shell target = 5 cm
- Source size = 2 x 4 x 2 cm^3
- Detector size = 5 cm in diameter and 5 cm long
- Distance from source center to wall = 221 cm
- Distance from detector to wall = 278 cm

This model is quite large and requires significant computation time in order to achieve statistically reliable results. If we examine the path of particles that reach the detector, we realize that most particles have to travel along the hole, the wall or within a few mean free paths in the vicinity of the hole. Particles traveling farther than a few mean free paths inside the wall have a very small chance being detected by the relatively small detector. Hence, it is reasonable to reduce the model size by cutting a large segment of the wall along x- and y- axes, while preserving the model dimension along the z-axis. The dimensions of the this small model (shown in Fig. 3) are summarized below:

- Overall size = 35 x 60 x 626 cm^3
- The other dimensions: same as the large model

To compare the full size and the small models, we use an energy dependent, isotropic source based on the D(d,n) reaction for 5 MeV deuterons, and estimate energy-dependent flux distributions along the z-axis, from the target to the detector. Figure 4 compares these distributions for different neutron energy ranges between ~3.7 and 8.0 MeV. As expected, the small model yields essentially the same results compared to the large model. This is very important for future analyses because the small model requires only 70% of the computational cost of the full size model.

ii) Examination of target shapes

Previous cross-section experiments have commonly used a sphere or spherical shell. However, since we are considering performing experiments with different size spheres, and further fabrication of spherical shells is costly, we have examined the effectiveness of other target shapes including rectangular and cylindrical shells. We have considered thicknesses of 5 and 10 cm, using two different evaluated nuclear data cross-section files for iron, and a 15.76 MeV isotropic source. Table 1 compares different targets based on the reaction rates of different reactions which occurred in the target.
With the new evaluated iron cross-section set, we observe similar behavior for cases with the same thickness. The total reaction rate increases by ~1.0 % in the 5-cm cases and ~1.5 % in the 10-cm cases. The elastic scattering rate increases by ~3.0 % in all cases and the inelastic scattering rate decreases by ~7.0 % in the 5-cm cases and ~8.0 % in the 10-cm cases. It is important to realize that reaction rates obtained from MCNP are the multiplication of flux and cross section after the simulation is carried out. Therefore, we have to take into account the fact that target thickness attenuates the flux. The sphere target provides the highest reaction rates, followed by the cylinder and the cube. Due to the curved surface in the sphere, a neutron has a higher probability of survival, compared to the cylinder and the cube, and thereby induces more reactions inside the target.

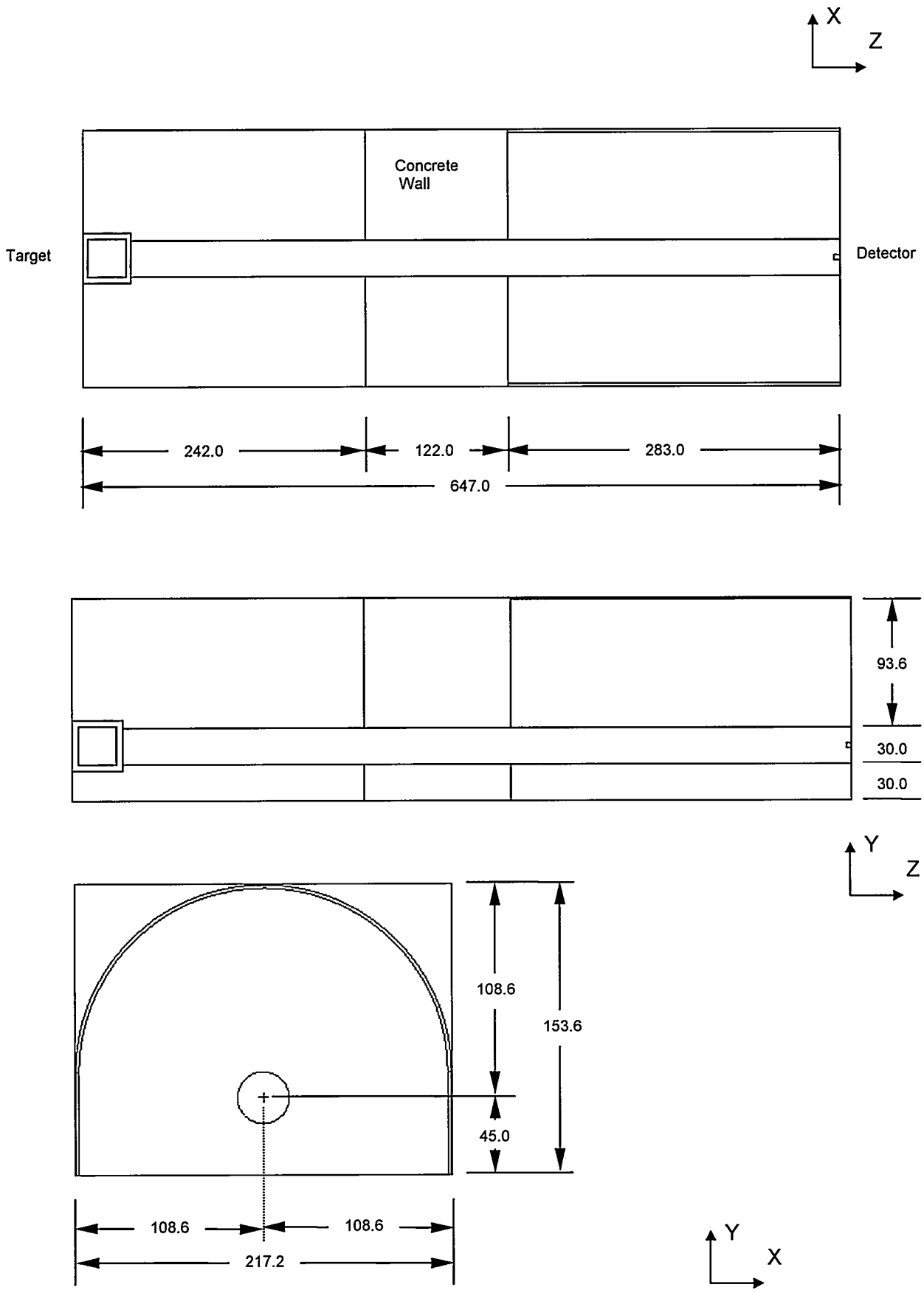

Figure 2: Schematic of the large model (units in cm)

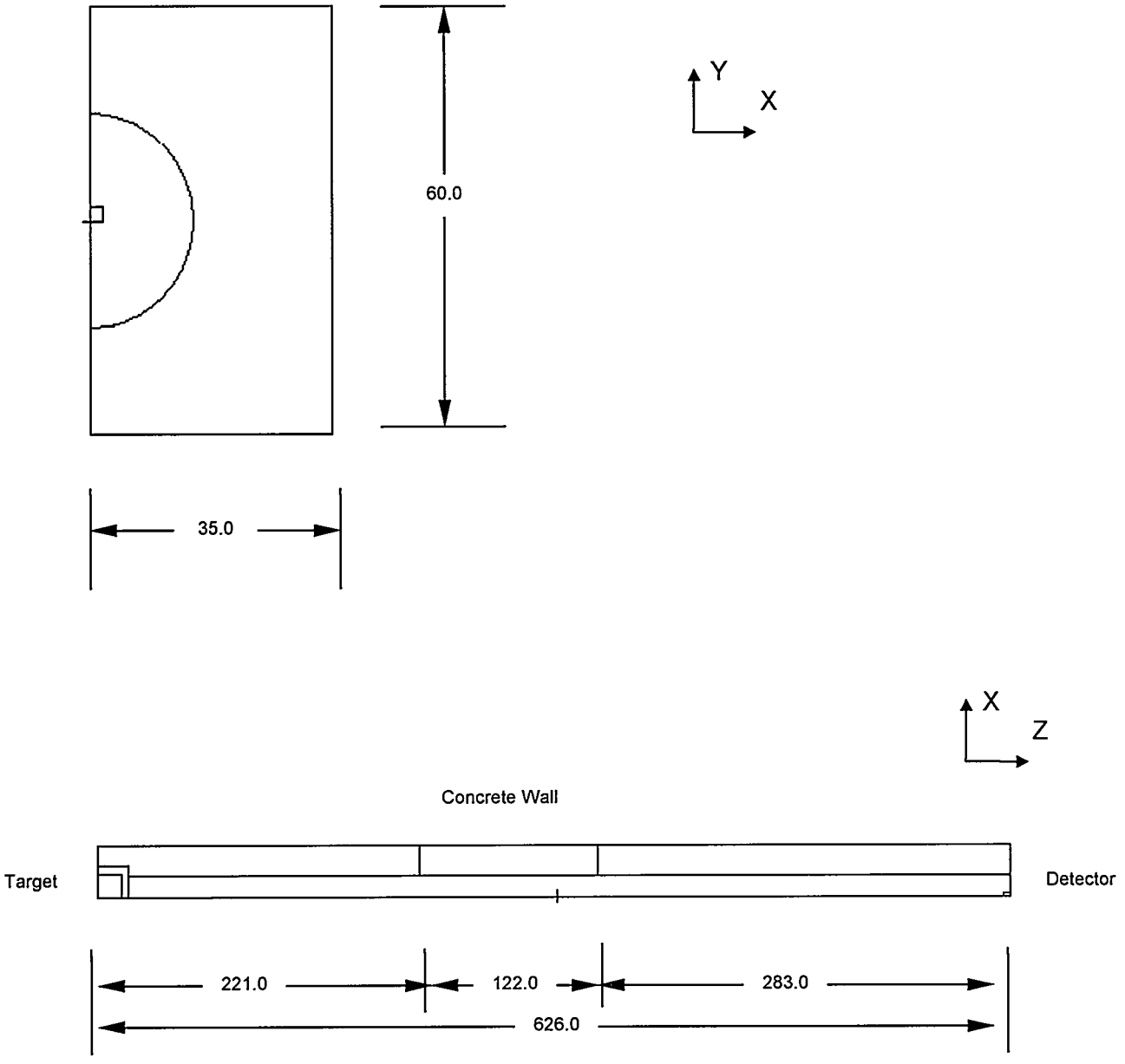

Figure 3: Schematic of the small model (units in cm)

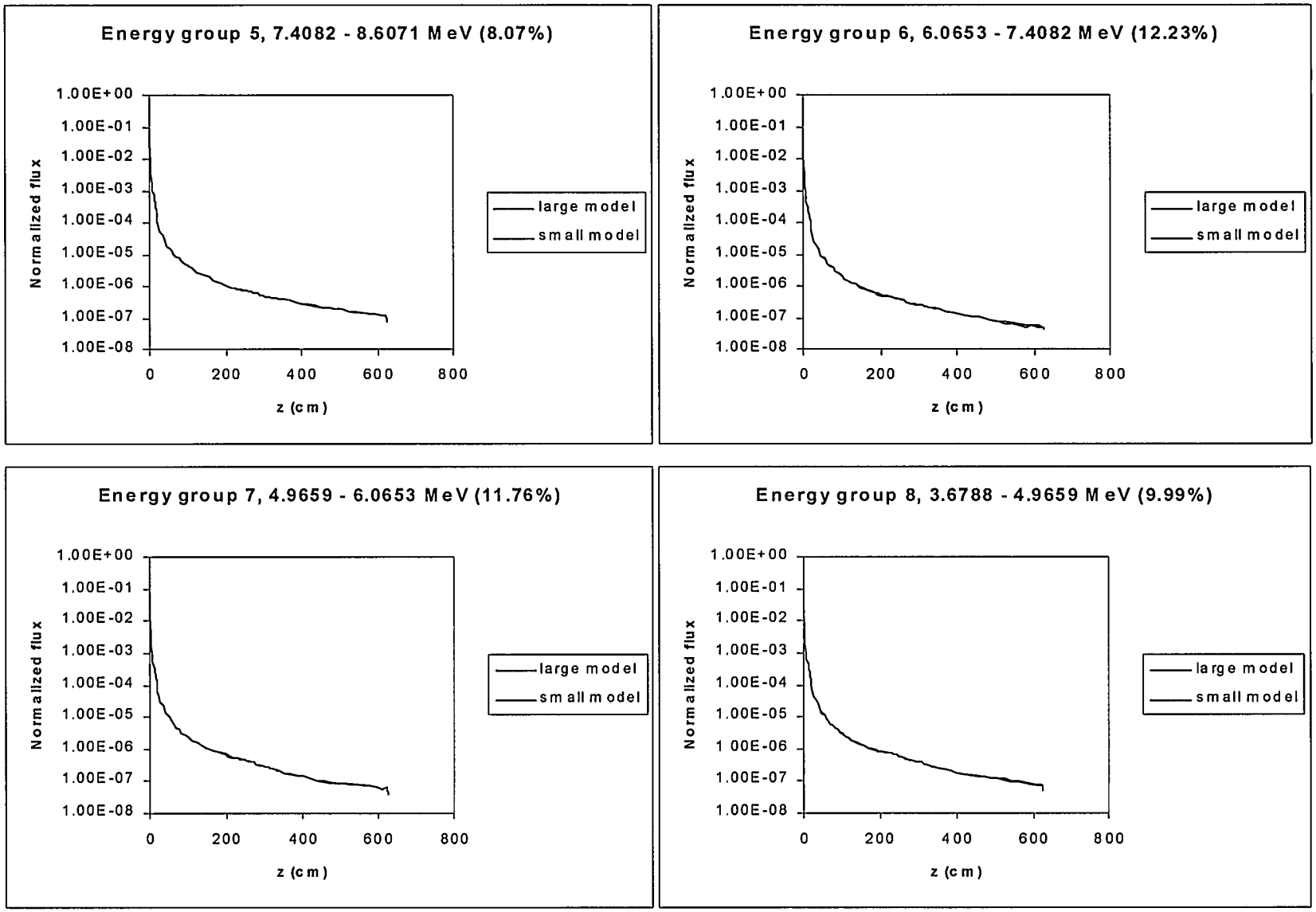

Figure 4: Flux distribution along the z-axis, using energy dependent, isotropic source based on 5 MeV D-D interaction

Table 1 Reaction rate of different target shapes, using isotropic, 15.76 MeV source with different cross-section files for Fe

Target shape: cube
Thickness: 5cm

reaction	ENDF/B	new xs	% diff
total	7.666E-05	7.739E-05	0.962
absorption	1.663E-06	1.610E-06	-3.167
elastic	5.505E-05	5.665E-05	2.916
n,2n	5.276E-06	5.253E-06	-0.438
n,3n	0	0	n/a
n,n'α	7.535E-08	6.466E-08	-14.194
n,n'p	1.368E-06	1.538E-06	12.431
n,n'd	0	0	n/a
n,n't	0	0	n/a
n,γ	6.860E-08	5.830E-08	-15.020
n,p	1.0707E-06	1.0365E-06	-3.197
n,d	8.247E-08	8.2348E-08	-0.147
n,t	1.0878E-09	1.1261E-09	3.521
n,3He	1.0879E-10	1.0808E-10	-0.654
n,α	4.3984E-07	4.318E-07	-1.828
inelastic	1.3227E-05	1.2275E-05	-7.195

Thickness: 10cm

reaction	ENDF/B	new xs	% diff
total	8.096E-05	8.225E-05	1.593
absorption	1.046E-06	9.958E-07	-4.827
elastic	6.563E-05	6.774E-05	3.220
n,2n	3.024E-06	3.001E-06	-0.764
n,3n	0	0	n/a
n,n'α	4.242E-08	3.633E-08	-14.363
n,n'p	7.804E-07	8.754E-07	12.181
n,n'd	0	0	n/a
n,n't	0	0	n/a
n,γ	9.7789E-08	8.1182E-08	-16.983
n,p	6.4229E-07	6.1636E-07	-4.037
n,d	4.7321E-08	4.7112E-08	-0.442
n,t	6.117E-10	6.3336E-10	3.542
n,3He	6.118E-11	6.0766E-11	-0.676
n,α	2.5819E-07	2 504E-07	-3.015
inelastic	1.0442E-05	9.6029E-06	-8.035

cylinder
Thickness: 5cm

reaction	ENDF/B	new xs	% diff
total	8.9692E-05	9.0558E-05	0.966
absorption	1.9997E-06	1.9383E-06	-3.070
elastic	6.3927E-05	6.58E-05	2.929
n,2n	6.3748E-06	6.3486E-06	-0.411
n,3n	0	0	n/a
n,n'α	9.1165E-08	7.8243E-08	-14.174
n,n'p	1.6539E-06	1.8598E-06	12.451
n,n'd	0	0	n/a
n,n't	0	0	n/a
n,γ	7.9017E-08	6.7361E-08	-14.752
n,p	1.2892E-06	1.2488E-06	-3.136
n,d	9.9627E-08	9.9504E-08	-0.124
n,t	1.3162E-09	1.3625E-09	3.524
n,3He	1.3163E-10	1.3078E-10	-0.648
n,α	5.304E-07	5.2118E-07	-1.738
inelastic	1.5645E-05	1.4533E-05	-7.108

Thickness: 10cm

reaction	ENDF/B	new xs	% diff
total	9.4443E-05	9.5791E-05	1.428
absorption	1.2754E-06	1.216E-06	-4.651
elastic	7.5872E-05	7.8214E-05	3.087
n,2n	3.7235E-06	3.6957E-06	-0.746
n,3n	0	0	n/a
n,n'α	5.2325E-08	4.4808E-08	-14.365
n,n'p	9.6132E-07	1.0785E-06	12.186
n,n'd	0	0	n/a
n,n't	0	0	n/a
n,γ	1.1118E-07	9.2595E-08	-16.717
n,p	7.8784E-07	7.566E-07	-3.966
n,d	5.826E-08	5.8012E-08	-0.426
n,t	7.5457E-10	7.8109E-10	3.514
n,3He	7.5469E-11	7.4942E-11	-0.699
n,α	3.1723E-07	3 0797E-07	-2.919
inelastic	1.2558E-05	1.1543E-05	-8.089

sphere
Thickness: 5cm

reaction	ENDF/B	new xs	% diff
total	1.167E-04	1.179E-04	1.051
absorption	2.7235E-06	2.6445E-06	-2.899
elastic	8.2099E-05	8.459E-05	3.033
n,2n	8.7498E-06	8.7188E-06	-0.355
n,3n	0	0	n/a
n,n'α	1.2544E-07	1.0771E-07	-14.133
n,n'p	2.2715E-06	2.5554E-06	12.498
n,n'd	0	0	n/a
n,n't	0	0	n/a
n,γ	9.9852E-08	8.5487E-08	-14.386
n,p	1.7593E-06	1.7061E-06	-3.019
n,d	1.3672E-07	1.3662E-07	-0.074
n,t	1.8112E-09	1.8753E-09	3.539
n,3He	1.8114E-10	1.800E-10	-0.627
n,α	7.2567E-07	7.1424E-07	-1.575
inelastic	2.0705E-05	1.9284E-05	-6.859

Thickness: 10cm

reaction	ENDF/B	new xs	% diff
total	1.219E-04	1.237E-04	1.490
absorption	1.7755E-06	1.6975E-06	-4.393
elastic	9.6351E-05	9.9488E-05	3.256
n,2n	5.2678E-06	5.2305E-06	-0.708
n,3n	0	0	n/a
n,n'α	7.4227E-08	6.3586E-08	-14.337
n,n'p	1.361E-06	1.5272E-06	12.212
n,n'd	0	0	n/a
n,n't	0	0	n/a
n,γ	1.3713E-07	1.1461E-07	-16.427
n,p	1.1075E-06	1.0647E-06	-3.866
n,d	8.2411E-08	8.2085E-08	-0.395
n,t	1.0706E-09	1.1082E-09	3.510
n,3He	1.0707E-10	1.0633E-10	-0.696
n,α	4.4726E-07	4.3488E-07	-2.768
inelastic	1.702E-05	1.5658E-05	-8.002

% diff = [(new-old)/old]x100

iii) Modification of MCNP for special tallying

A possible difficulty in determining the inelastic scattering cross-sections is the fact that experimentally it may be difficult to accurately separate the groups of inelastically scattered neutrons detected at the detector. This type of identification, however, is possible with simulation methods, but it is not readily feasible with the standard codes such as MCNP. Hence, we have modified the MCNP code by introducing new counters and flags in four routines including *acecol.f, hstory.f, trnspt.f,* and *mcnp.f.*

iv) Use of the modified MCNP for design optimization

The first use of the modified code is for fine-tuning our experimental setup; here, we have examined the placement of the detector. For this, we have developed a simplified test model consisting of a target slab of 5 cm thickness, a parallel beam from a source of size 2x2x2 cm^3 ,a neutron energy of 8 MeV, and a detector of 2 cm diameter. The source was placed 10 cm in front of the target and the detector was placed 15 cm in the back of the target.

First, as a verification step, we have determined the fraction of inelastic scattering within the target. It was concluded that for an 8 MeV mono-directional source, ~33.5% of scattering interactions are inelastic. This is consistent with the behavior of the inelastic versus the elastic cross-sections shown in Fig. 5, and also our previous simulations using the standard MCNP code.

Second, we plan to examine the placement of the detector. When the detector is placed in the center of the beam, the uncollided neutrons are the majority of the detected particles and are directly related to the neutron total cross section. By using time-of-flight techniques, the inelastically scattered neutrons can be separated from the intense uncollided and elastically scattered neutrons. Additional information can be obtained for the detector located outside of the beam. We will consider three detector configurations: along the axis, 1 cm off the axis, and 3 cm off the axis.

Using the new version of MCNP, we are reexamining our previous results related to target shape, thickness and location.

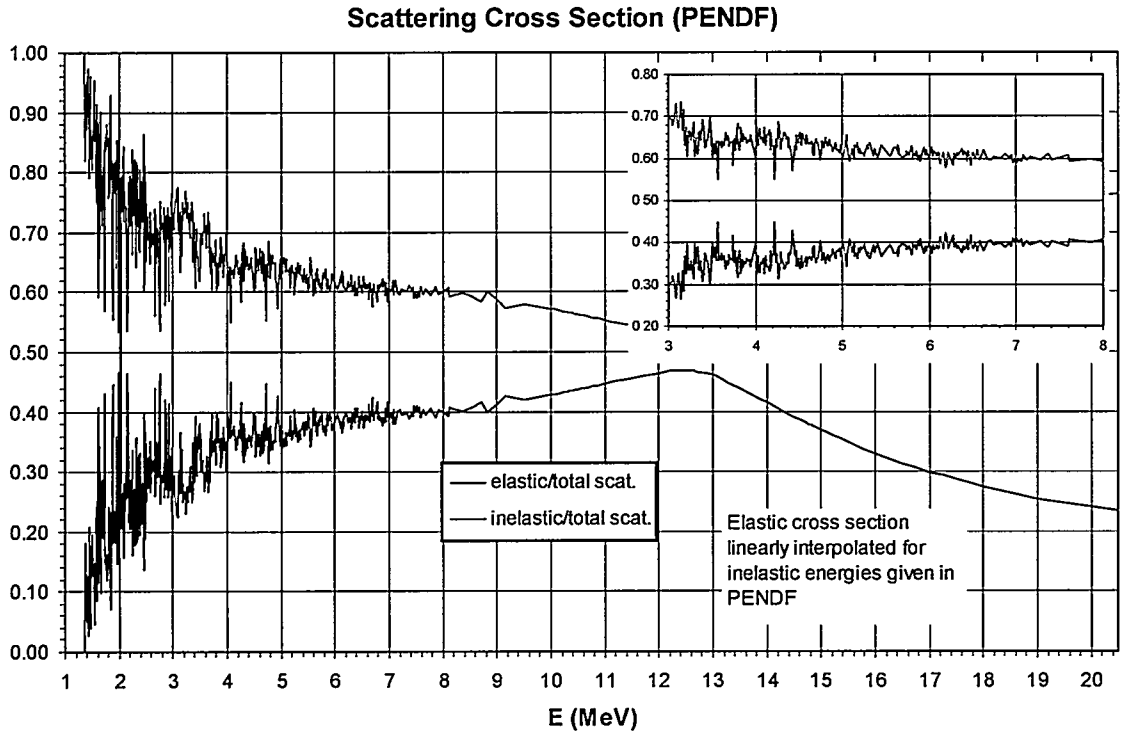

Figure 5: Elastic and inelastic scattering of Iron (from ENDF/B-VI library)

v) Development of 3-D PENTRAN™ models using a new method for generation of angular quadrature sets

The discrete ordinates method has the advantage over the Monte Carlo method of providing more detailed information (E.g., 3-D flux distribution) with relatively small computational cost. Hence, it is best suited for performing sensitivity analyses. We are planning to perform several sensitivity studies to investigate the effect of different target shapes and thicknesses, different source distributions and geometric setups. For this purpose, an efficient, yet accurate S_N model is necessary. Furthermore, we will be utilizing the S_N models for generation of multigroup cross-section libraries and testing the new iron cross-sections.

For S_N modeling of the experimental setup, we have developed several forward and adjoint PENTRAN models in pursuit of performing accurate and efficient simulations. This is a very large problem with three-dimensional geometry and a relatively large particle energy range, which requires significant computational resources (i.e., memory and CPU). Furthermore, most of the problem domain is composed of air, which causes numerical difficulties called "ray effects". In order to overcome these difficulties, we have taken the following measures: i) We are utilizing the PENTRAN parallel S_N code and the San Diego Supercomputing Center (IBM SP2) to run the problems with quick turn-around times; ii) We have developed and implemented new angular quadrature sets to mitigate the ray effects. The new quadrature sets allow a larger number of directions (compared to the standard level-symmetric quadrature sets) and angular refinements in the directions of interest; iii) We have developed new methodologies including a ray tracing method and coupling of forward and adjoint calculations. Here, we discuss the models and the methodologies we have developed for the S_N calculations.

Large Model

We first developed a 3-D PENTRAN model that replicates the experimental setup considering symmetry conditions on the x=0.0 cm and z=0.0 cm surfaces and vacuum boundary condition on remaining surfaces. Figure 6 shows the volumetric material distribution. The model extends 626.0 cm in the z-axis, 108.0 cm in the x- and y-axes, including source, the iron shell, wall, tunnel and detector. For this model, we have used the highest level-symmetric quadrature S_{20}. We have generated cross-sections using the BUGLE-96 library with P_5 anisotropic scattering order. We have partitioned this model into 8 angular and 8 spatial sub-domains and run it on 64 processors of IBM-SP2, with a memory requirement of ~500 Mbytes/processor.

We have performed a 1-group calculation and obtained the flux distribution for 14 MeV neutrons. As is seen in Figure 7, the flux distribution is not smooth, especially in the void regions; it suffers significantly from ray-effects. We quickly have realized that the level-symmetric quadrature set, which is limited to 440 directions in 3-D, is not adequate for this large model. Hence, we have developed new angular quadrature sets including *Equal Weight* and *Ordinates Splitting*. These new angular quadrature sets do not have

limitations on the number of directions; the simulations can be performed using as many directions as the computational resources allow. The ordinates splitting method provides refinement in the direction of interest. Particularly, for this problem, the neutrons move along the $+z$ axis, therefore, we can add more directions *only* along this axis, thereby saving significant memory and CPU time.
In order to test the effectiveness of the new quadrature sets, we have cropped the large model in x-, y- and z- directions and developed a smaller model.

Small Model

Figure 8 shows the small model used for investigation of different quadrature sets and orders. This model extends 100.0 cm in the z-axis, 35.0 cm in the x- and 60 cm y-axis, including source and the iron shell. Depending on the quadrature and splitting order, we have performed the tests on a range of 20 to 56 processors requiring ~200 to ~500 Mbytes/processor.

We have obtained flux distribution for 14 MeV neutrons and compared the results with Monte Carlo calculations. Figure 9 shows the flux distribution along the z-axis at x=1.0 cm and y=1.0 cm for different quadrature sets and orders. Cases 1-7 refer to Equal Weight S_{30} and Cases 8-11 refer to Level –Symmetric S_{20}, both sets with different splitting options. We have added extra directions around the first direction (closest direction to the z-axis) of the S_{30} quadrature set in Cases 2-8, excluding Case 5. We observe that in most of the cases, the discrete ordinates solution starts departing from the Monte Carlo solution at z=~35 cm. However, for Case 7, where there are 9 extra directions (3x3) around the first direction, we get very good agreement with the Monte Carlo solution. With this study, we concluded that Equal Weight S_{30} with 3x3 splitting is adequate for this model.

vi) Development of new methodologies based on the PENTRAN S_N, ray-tracing in the air, and coupling of forward and adjoint S_N solutions

To reduce the large memory and CPU requirements in the S_N simulations, we have considered two new methodologies in which we partition the model into regions and perform separate calculations for these regions. Fig. 10 depicts the two methodologies.

In the first method, we perform an S_N calculation in the region from source to the outer surface of the iron shell (z=0.0 cm to 21.0 cm). We, then project the angular fluxes from the surface of the iron shell up to the wall (z=21.0 cm to z=221.0 cm) using a ray tracing method and geometric attenuation. We have developed a computer code (PEN_RT, see Appendix) for performing this projection. Inside the wall, we again perform an S_N calculation using the projected fluxes as boundary surface source and obtain the angular fluxes on the outer surface. Using the ray tracing method, angular fluxes are then transported in the region between the wall and the detector (z=343. cm to 626. cm).

In the second method, we utilize the adjoint function instead of the ray tracing method in the last region between the wall and the detector. Adjoint function offers more physical

information as to what regions and energy groups are important for the detector response. In this method, the flux on the surface of the wall is coupled with the adjoint function to calculate the response at the detector:

$$R = \sum_{g=1}^{G} \sum_{i,j,k} \Phi_{i,j,k,g} \Phi^{+}_{i,j,k,g} \qquad (1)$$

Here, *i, j, k* represent the spatial mesh indices and *g* represents the energy group index. In both methods, the computational effort is reduced by dealing only with a segment of the problem at a time.

Preliminary Forward and Adjoint Calculations

We have performed preliminary forward and adjoint calculations to verify the discrete ordinates results. Figure 11a shows the extended small model referred to as *Model A* for forward calculations. This model extends to the outer surface of the wall (z=343. cm). Figure 11b shows the adjoint model for the region between z=335. cm and z=626. cm.

Using multigroup source obtained from D-D interaction (5MeV Projectile), we have obtained 3-D flux distributions. Note that, we have used S_{30} (Equal Weight) angular quadrature set with 3x3 by splitting along the z-direction. As seen in Figures 12 a-b, the flux distribution is quite smooth and ray-effects are greatly mitigated with the new quadrature set. In Figures 13 a-b, we present comparisons with Monte Carlo solutions. We observe that, the S_N solution agrees well with the Monte Carlo solution, especially for lower energy particles.

For adjoint calculations, we have placed a unit source at the detector as the adjoint source and obtained 3-D adjoint function distribution for fast neutrons. Figure 14 shows that particles in the vicinity of the detector are most important to the detector response and the importance decreases exponentially as we move away from the detector. Using Equation 1, we have coupled the adjoint function and the forward flux at the wall interface and calculated the response for both Large and Small models. We have observed ~6% difference between the Large and Small model results. We have concluded that the size (x and y) of the Small model is adequate for accurate results.

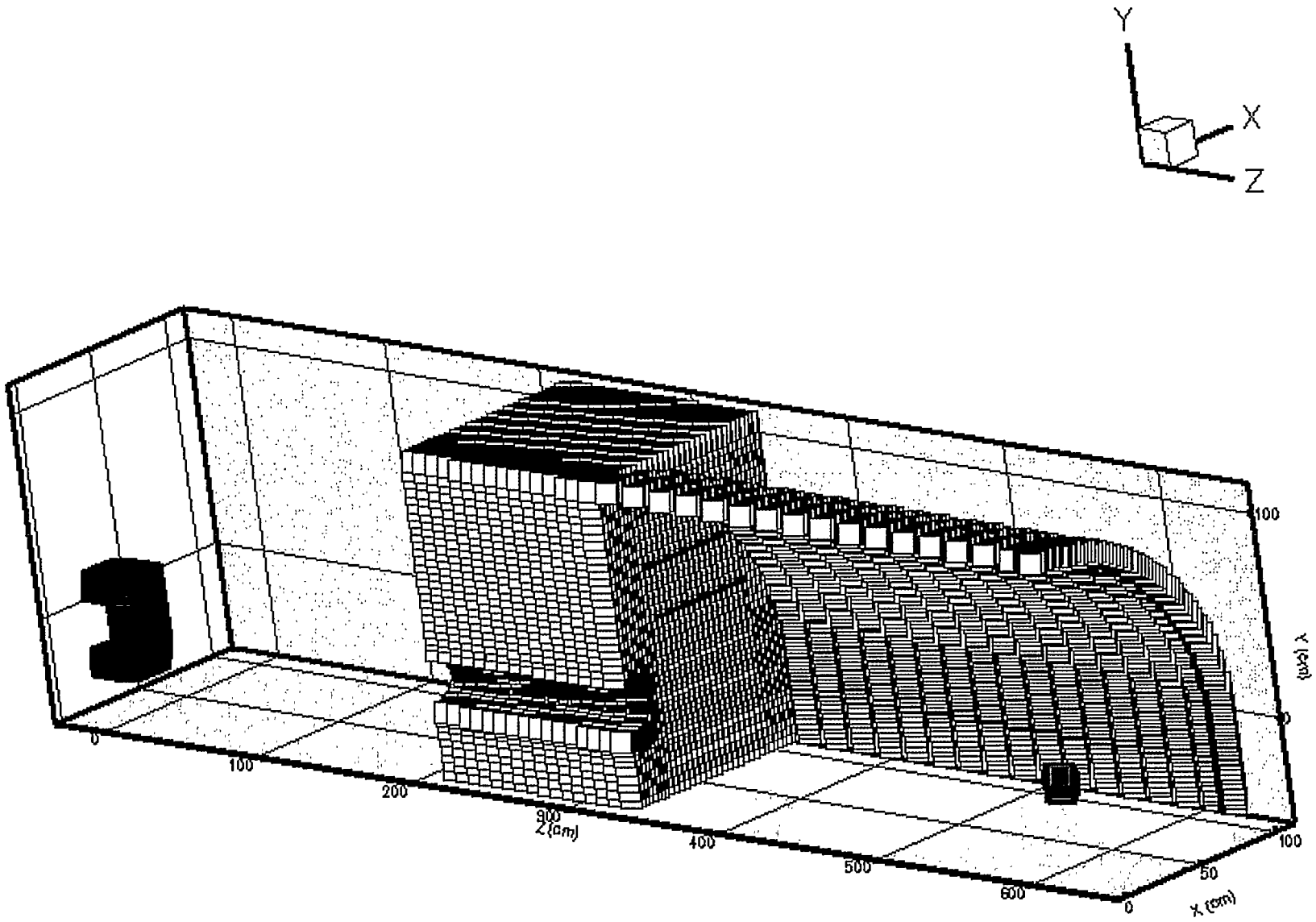

Figure 6: Material Distribution in Large Model

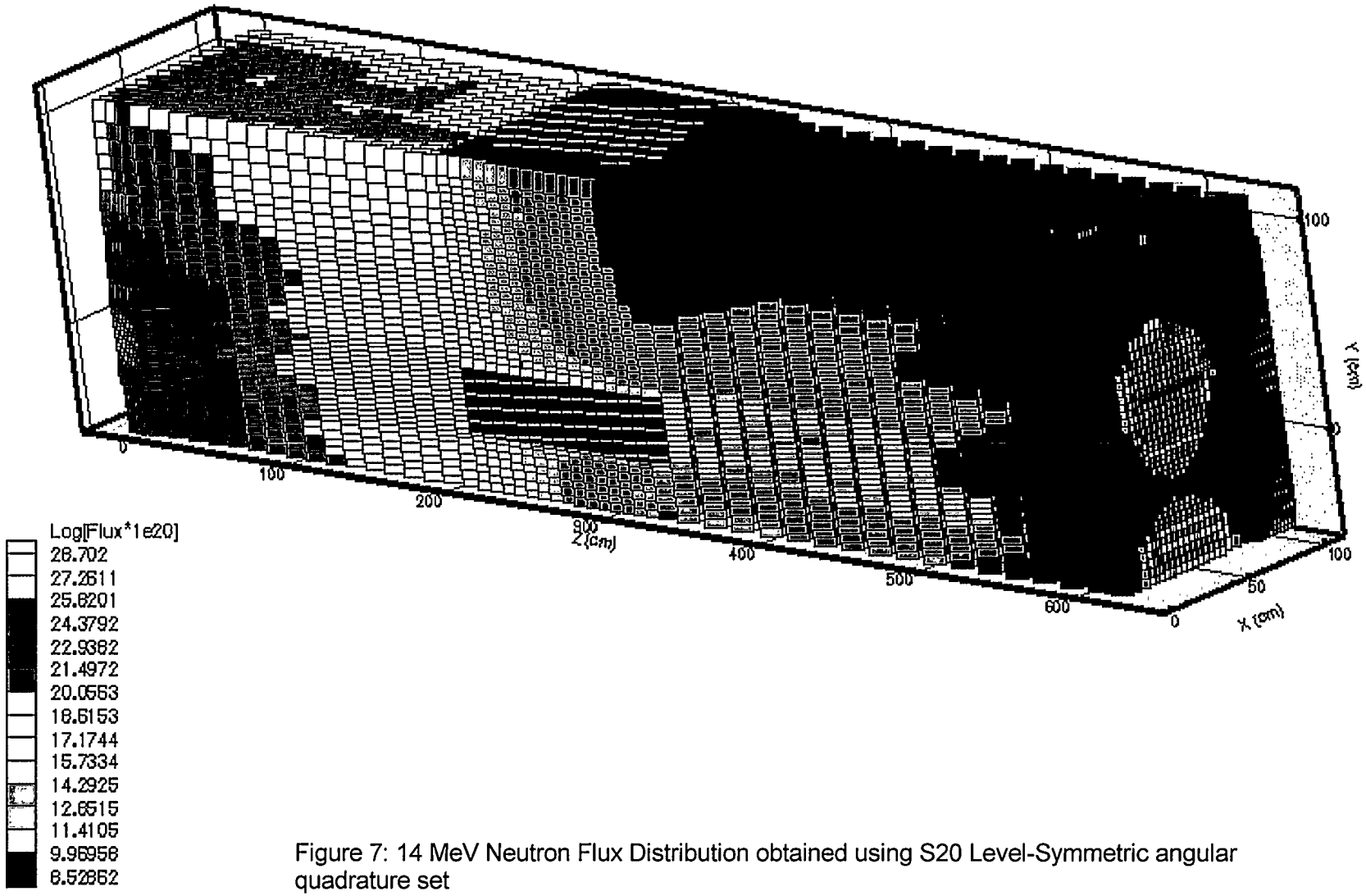

Figure 7: 14 MeV Neutron Flux Distribution obtained using S20 Level-Symmetric angular quadrature set

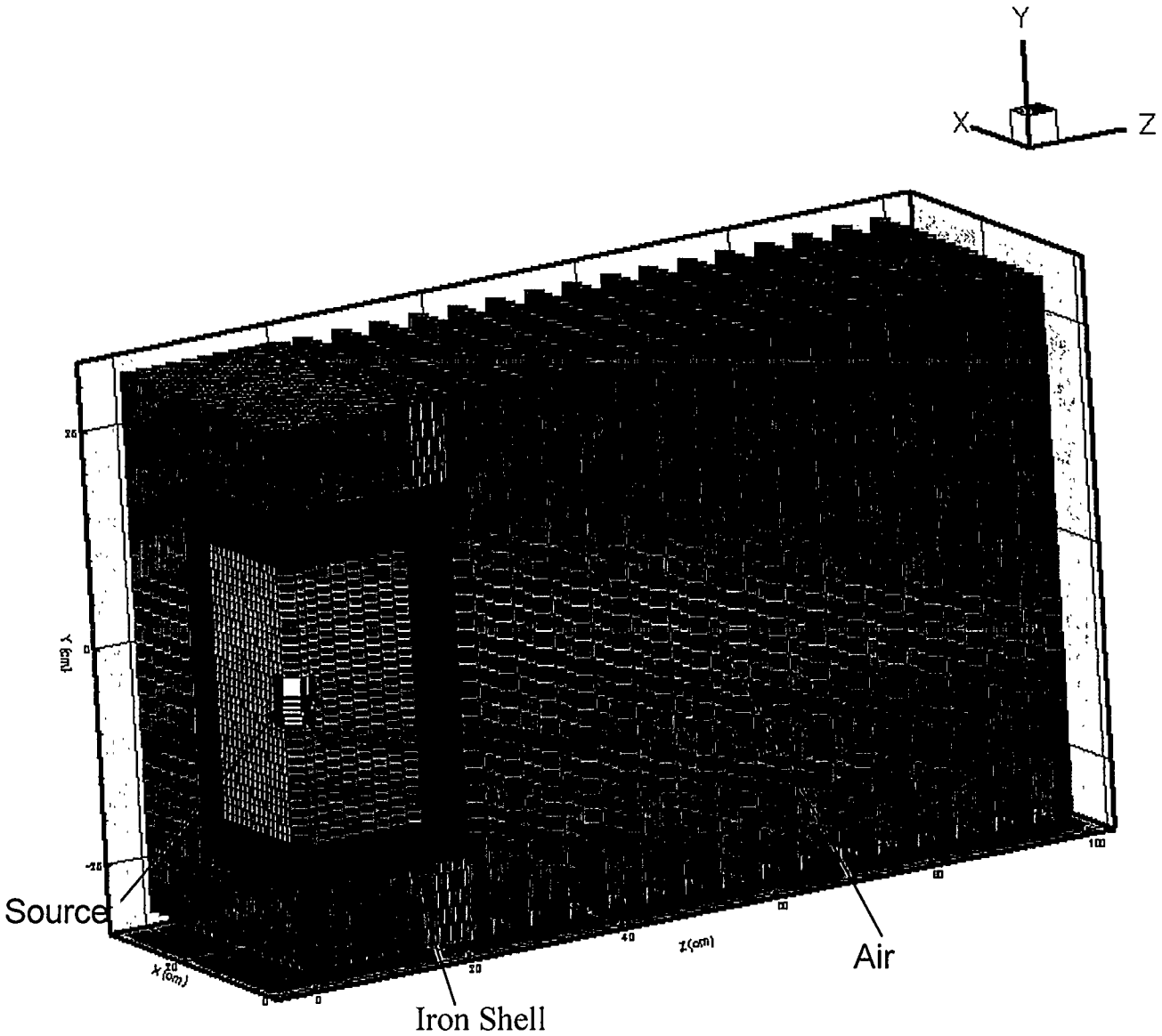

Figure 8: Small Model used for investigating different quadrature sets and orders

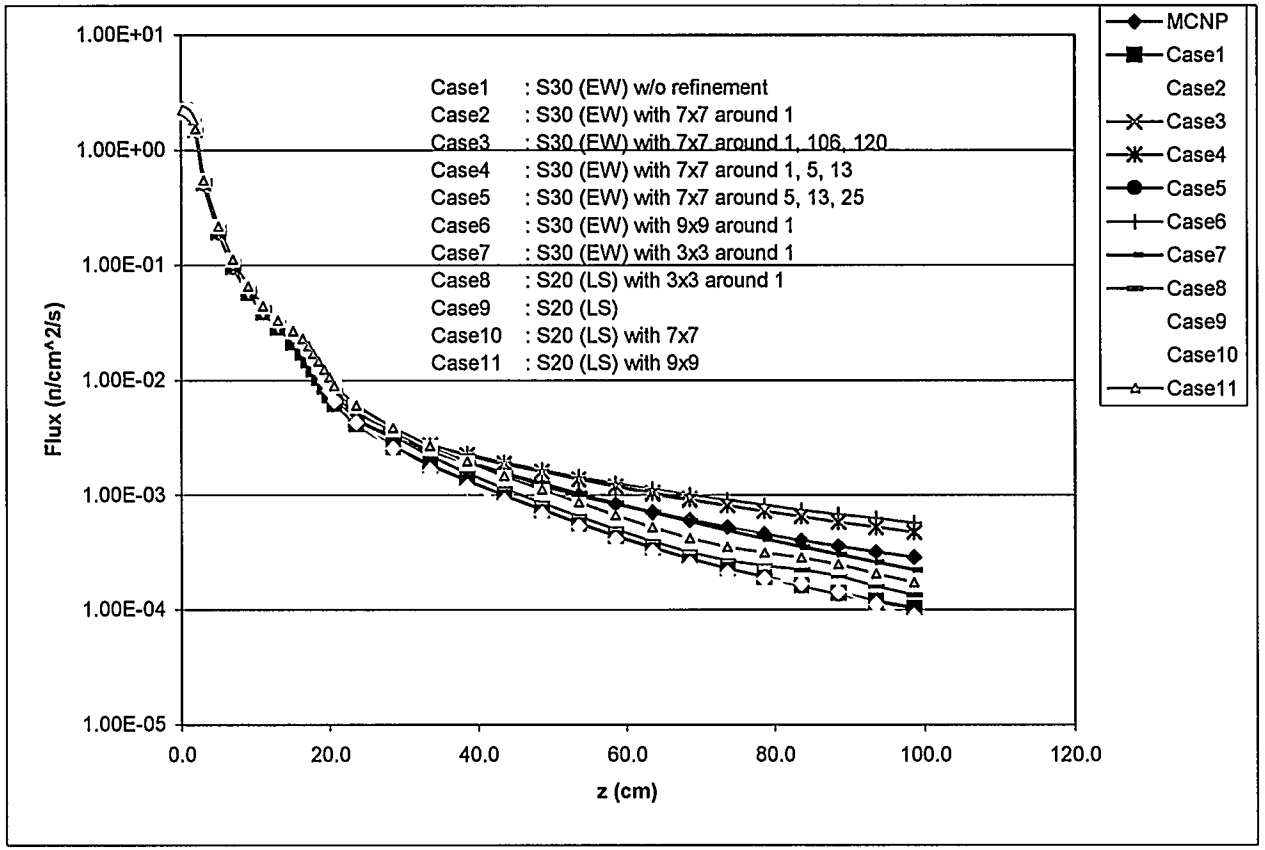

Figure 9: Comparison of different quadrature sets and orders with MCNP

Figure 10: Schematic of the new methodologies

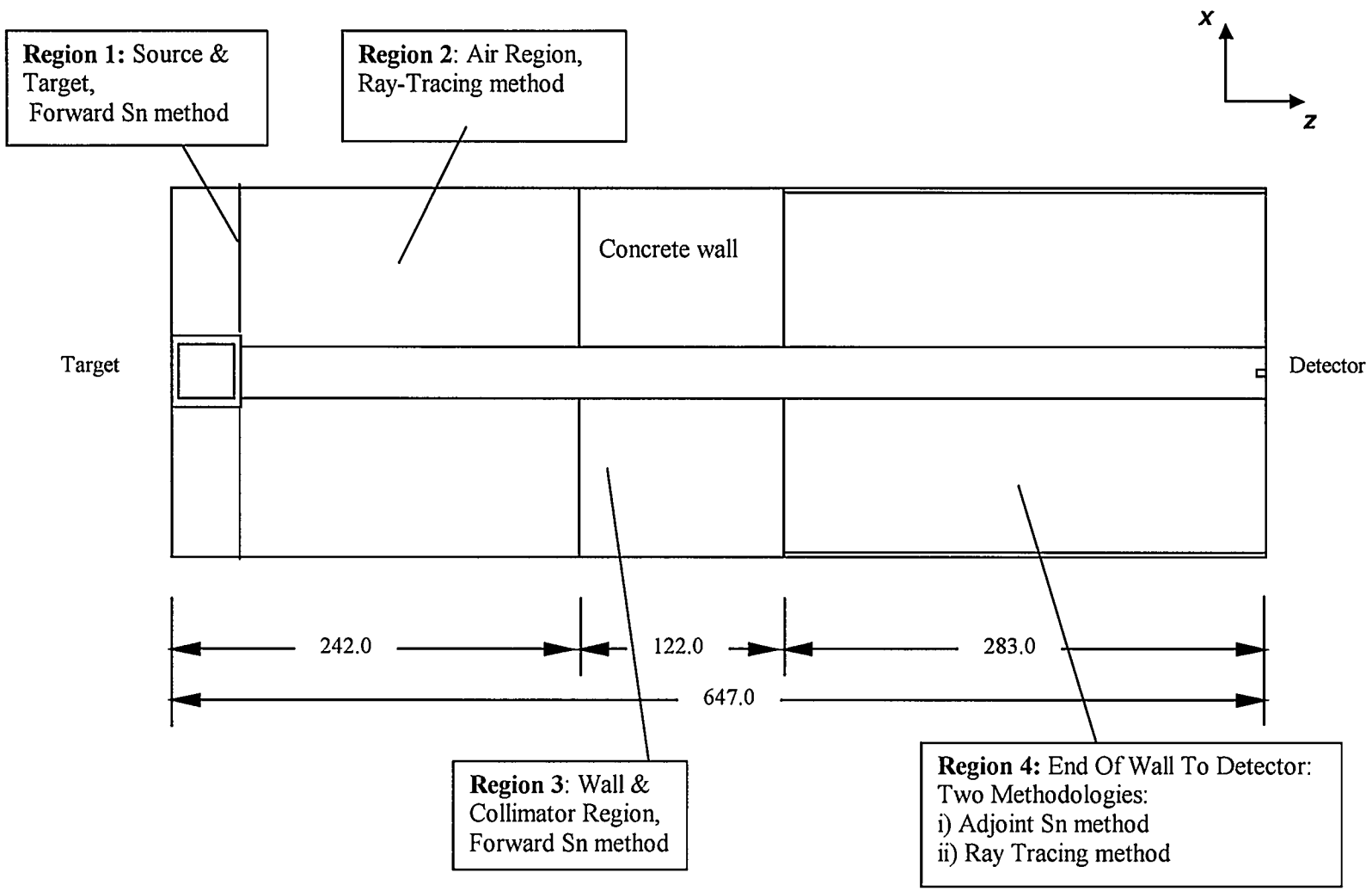

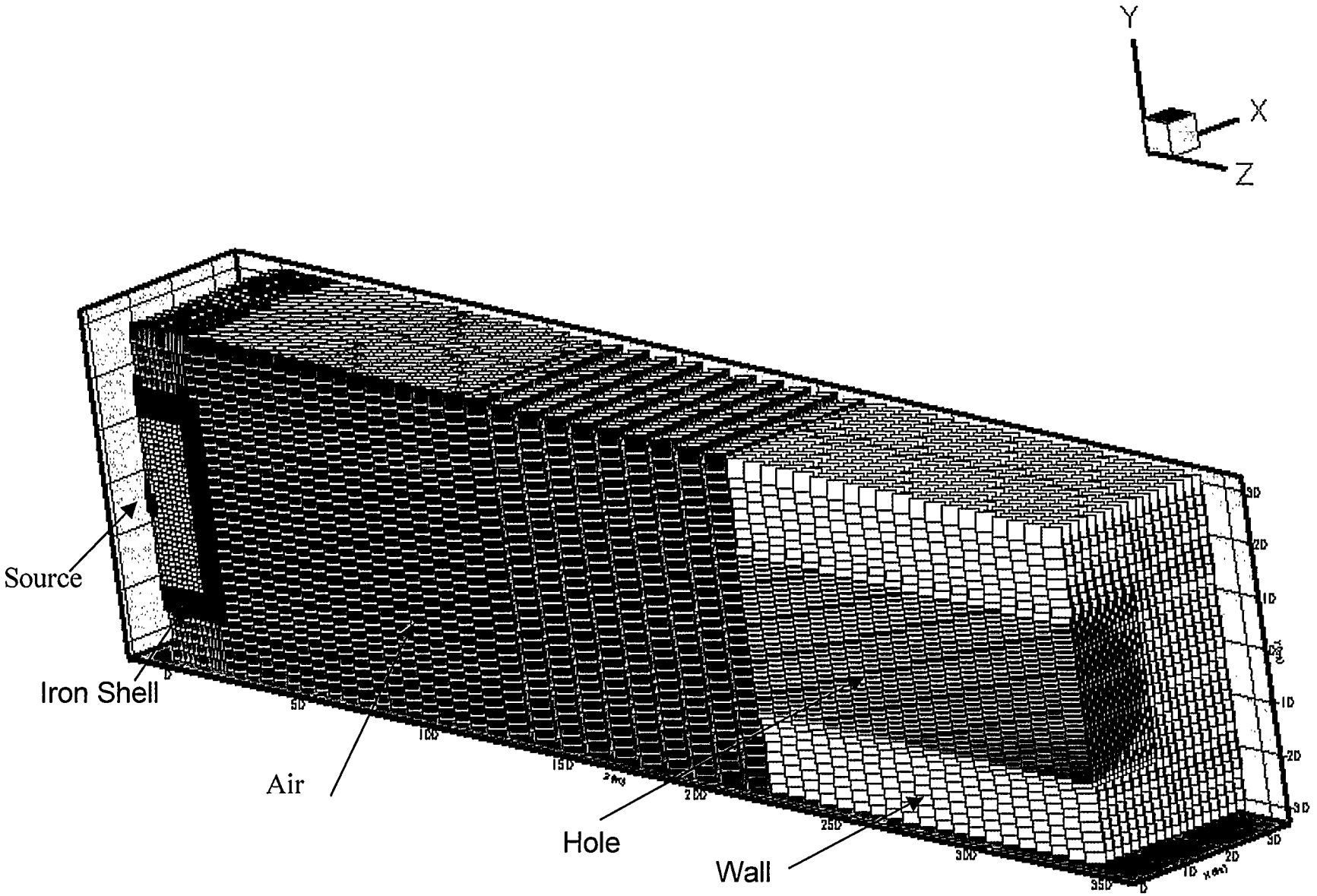

Figure 11a: Model A for Forward Calculations

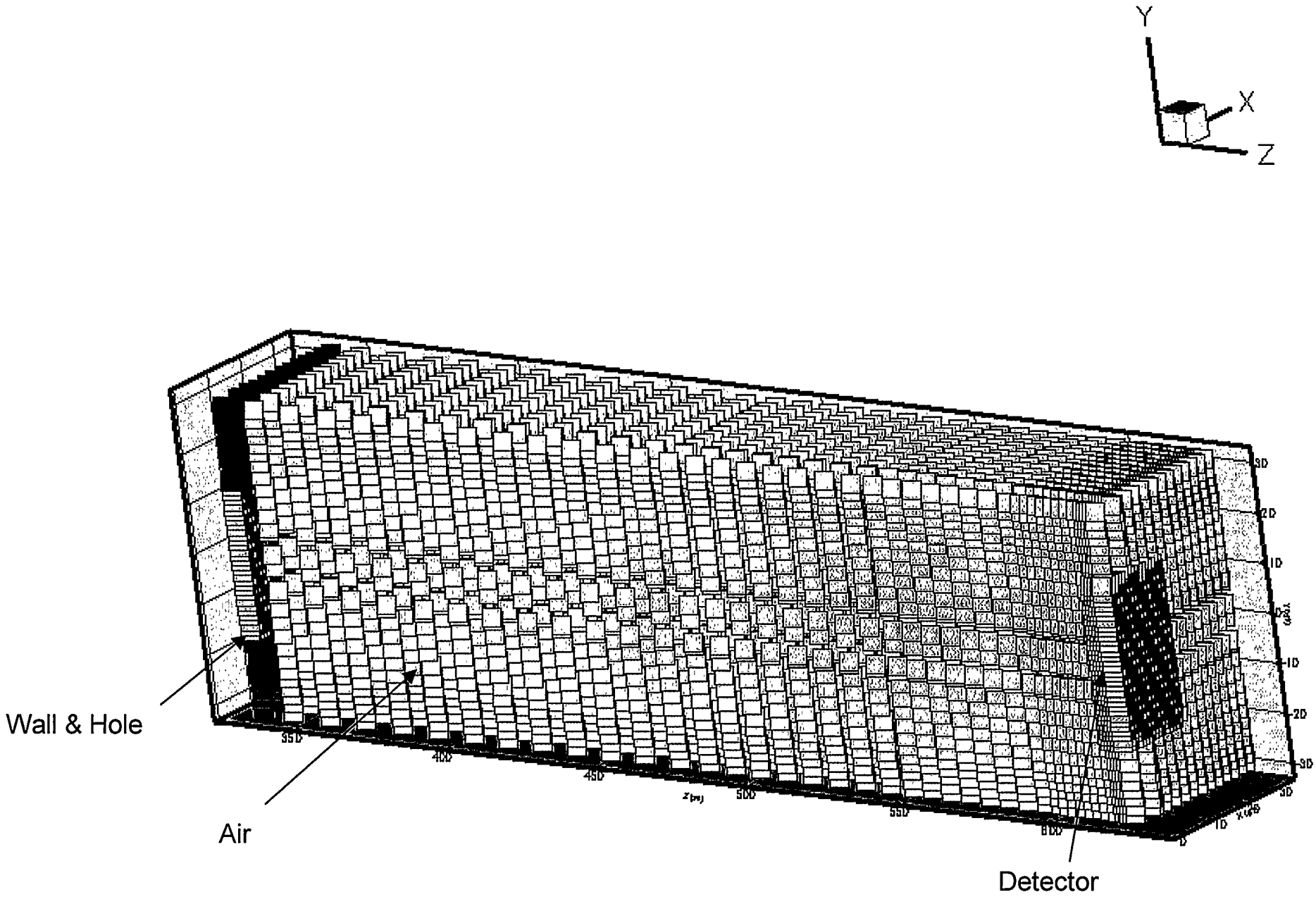

Figure 11b: Model B for Adjoint Calculations

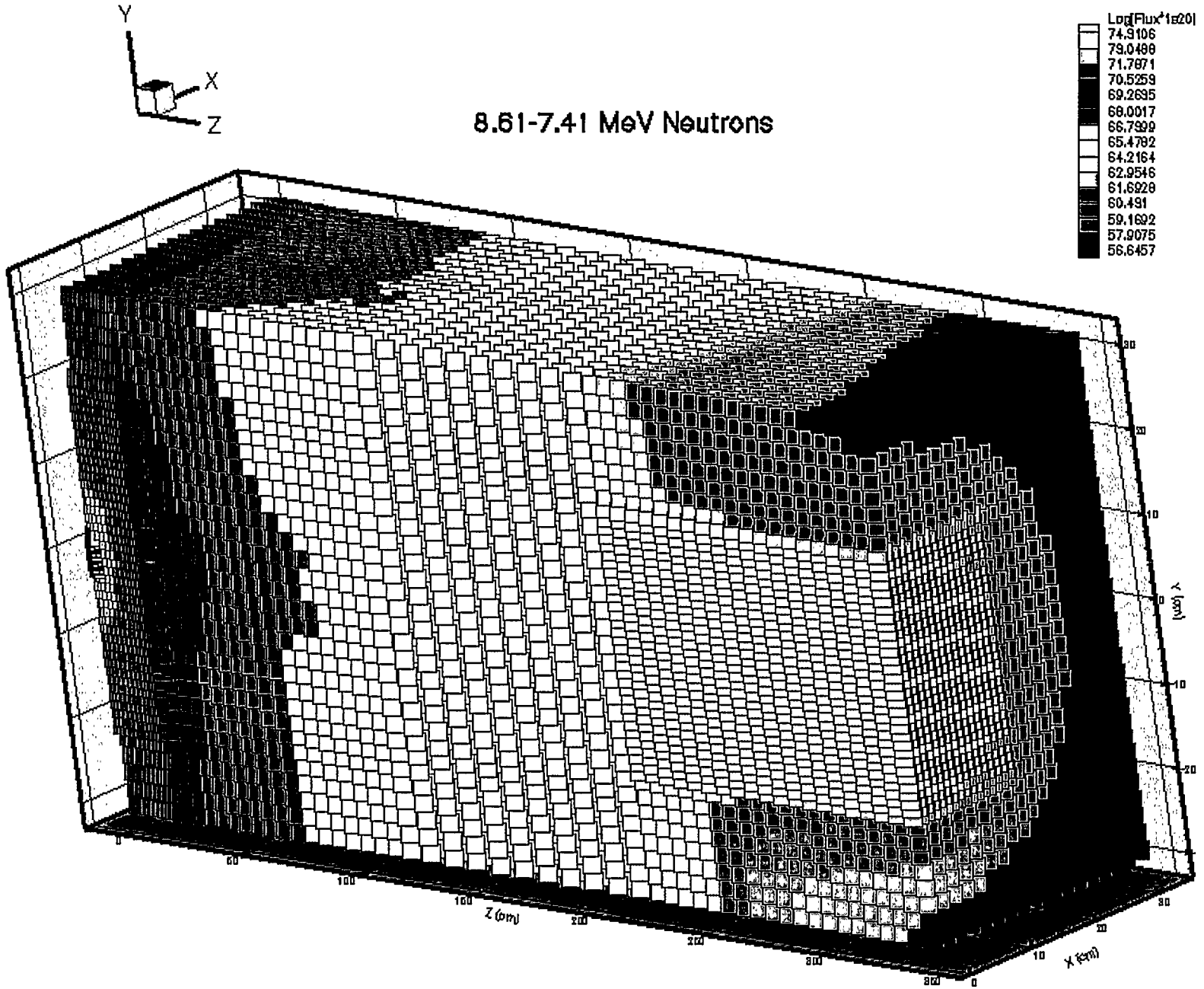

Figure 12a: 3-D Flux Distribution of 8.61-7.41 MeV Neutrons

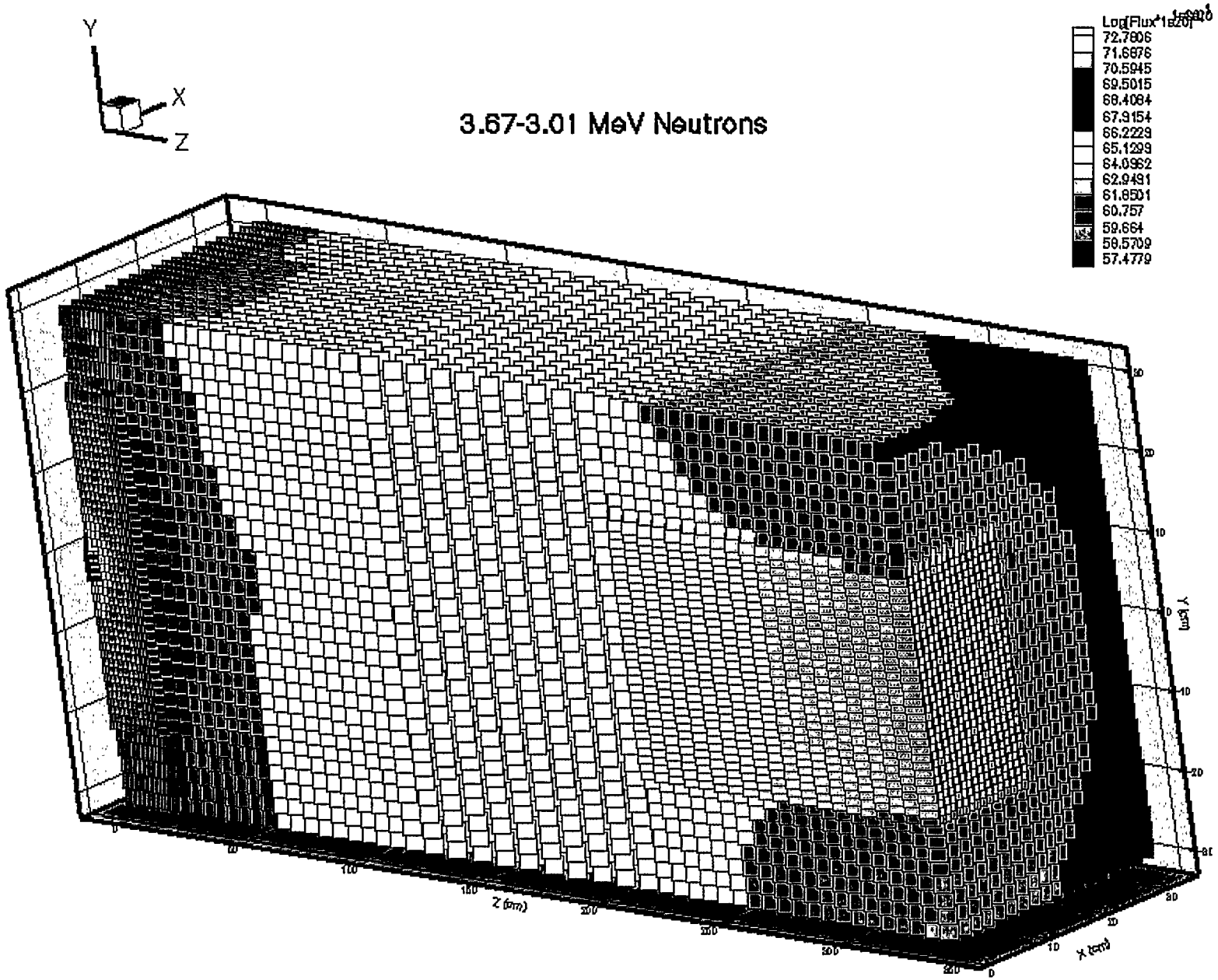

Figure 12b: 3-D Flux Distribution of 3.67-3.01 MeV Neutrons

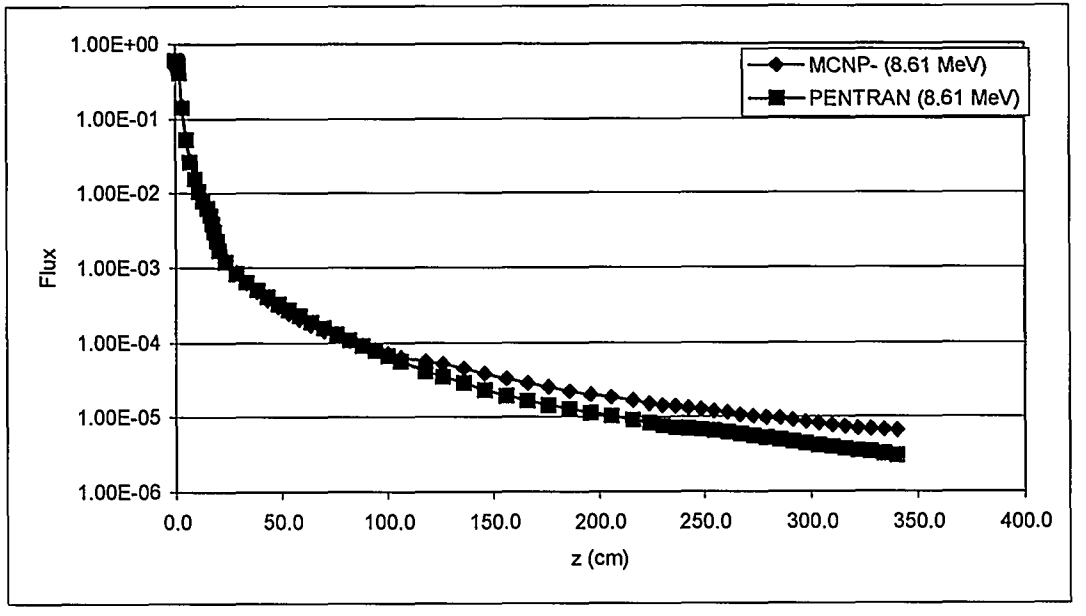

Figure 13a: Comparison of PENTRAN and MCNP results for 8.61 MeV Neutrons

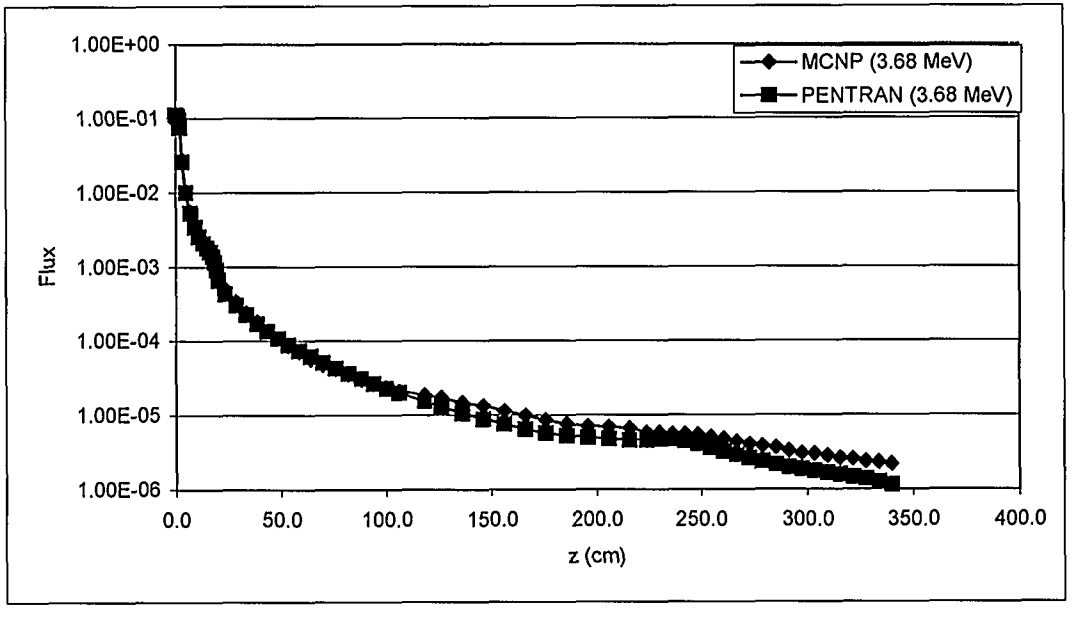

Figure 13b: Comparison of PENTRAN and MCNP results for 3.68 MeV Neutrons

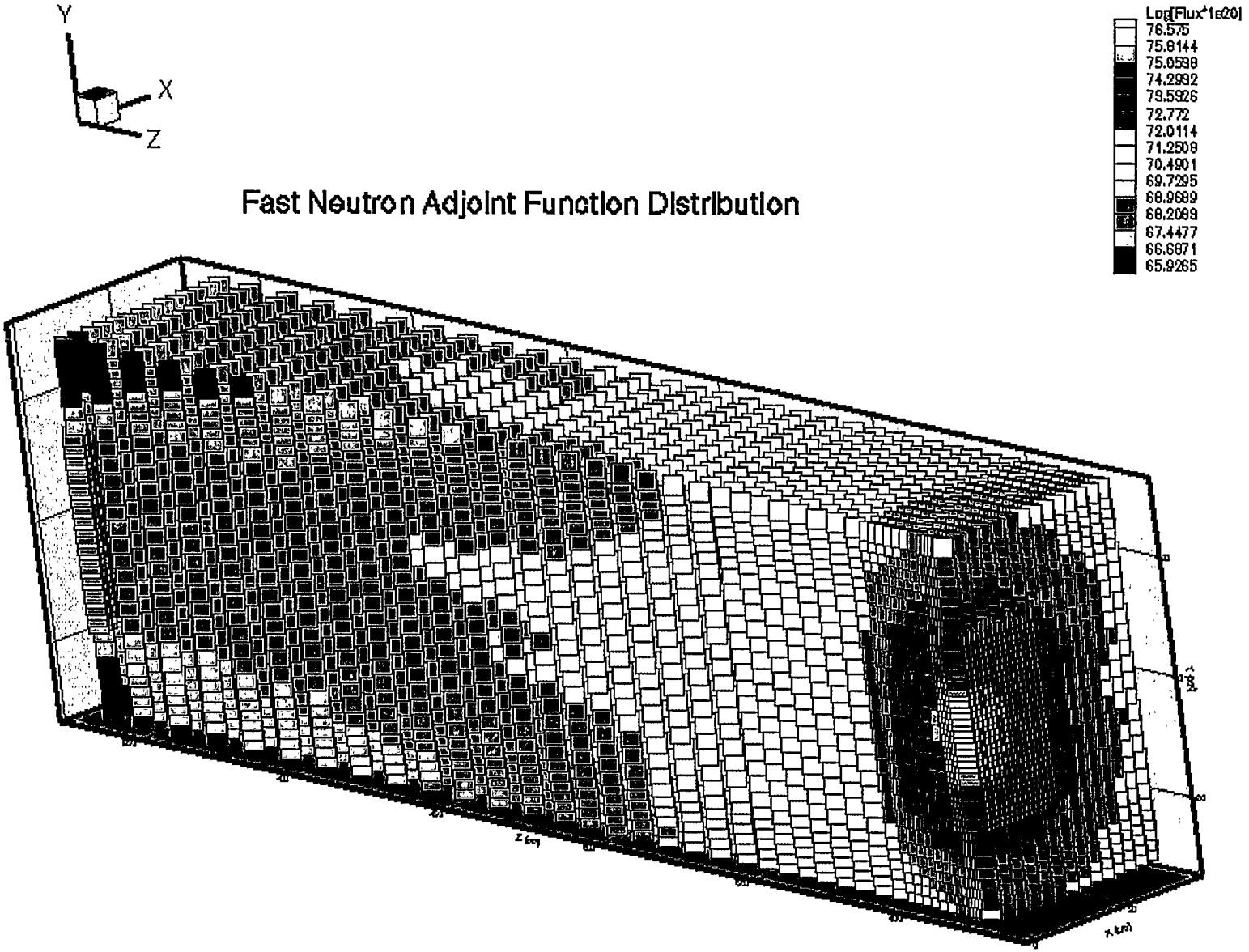

Figure 14: Adjoint function distribution of fast Neutrons

Appendix

Development of a computer program for ray-tracing (PEN_RT) within the air:

PEN_RT performs the following functions:

1.) Assumes a $\frac{1}{r^2}$ geometric flux attenuation in the air.

2.) Utilizes the PENTRAN angular flux output file option as an input file.

3.) Traces the angular fluxes obtained from PENTRAN in an (x,y) plane to another (x,y) plane (mesh grid) a fixed z distance away. (Note: we consider only $\frac{1}{r^2}$ geometric attenuation in the air.)

4.) Calculates scalar flux as an (x,y) mesh averaged quantity for each group. Meshes are variable coarse meshes in x,y, with a fixed number of fine meshes in x,y per coarse mesh, similar to the PENTRAN code for compatability.

5.) Prepares an output file (containing scalar fluxes) for PENTRAN.